ACS APPLIED MATERIALS & INTERFACES

www.acsami.org

Research Article

Highly Stable Buffer-Based Zinc Oxide/Reduced Graphene Oxide Nanosurface Chemistry for Rapid Immunosensing of SARS-CoV-2 Antigens

Fatemeh Haghayegh,[‖] Razieh Salahandish,[‖] Mohsen Hassani, and Amir Sanati-Nezhad*

Cite This: *ACS Appl. Mater. Interfaces* 2022, 14, 10844−10855

Read Online

ACCESS | Metrics & More | Article Recommendations | Supporting Information

ABSTRACT: The widespread and long-lasting effect of the COVID-19 pandemic has called attention to the significance of technological advances in the rapid diagnosis of SARS-CoV-2 virus. This study reports the use of a highly stable buffer-based zinc oxide/reduced graphene oxide (bbZnO/rGO) nanocomposite coated on carbon screen-printed electrodes for electrochemical immuno-biosensing of SARS-CoV-2 nuelocapsid (N-) protein antigens in spiked and clinical samples. The incorporation of a salt-based (ionic) matrix for uniform dispersion of the nanomixture eliminates multistep nanomaterial synthesis on the surface of the electrode and enables a stable single-step sensor nanocoating. The immuno-biosensor provides a limit of detection of 21 fg/mL over a linear range of 1−10 000 pg/mL and exhibits a sensitivity of 32.07 ohms·mL/pg·mm^2 for detection of N-protein in spiked samples. The N-protein biosensor is successful in discriminating positive and negative clinical samples within 15 min, demonstrating its proof of concept used as a COVID-19 rapid antigen test.

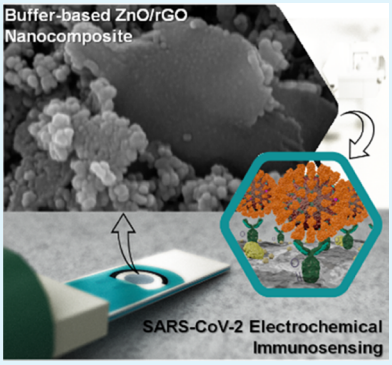

KEYWORDS: *SARS-CoV-2, antigen testing, nucleocapsid proteins, zinc oxide, reduced graphene oxide, electrochemical immunosensing*

1. INTRODUCTION

With the outbreak of the COVID-19 pandemic globally, the urgent need for rapid and accurate diagnostic tests has been underlined to prevent further disease spread.[1−5] While detecting viral RNAs through real-time reverse-transcriptase-polymerase chain reaction (rRT-PCR) is the gold standard diagnostic technique,[6,7] growing demands for rapid diagnosis, through the integration of detection techniques and fluid handing chips,[8] are highlighted for controlling the spread, which can be enabled through the advancement of immuno-assays[9−11] and nanodiagnostics.[12] In this regard, methods working based on the distinct antibody (Ab)/antigen viral biomarkers have become prevalently adopted, especially when rapid and early detection is of interest.[5,13,14] Taking advantage of the structural proteins of the SARS-CoV-2 virus, highly specific monoclonal antibodies[15,16] are becoming commonly employed for the development of immunoassays.[17,18] Among different structural proteins, Nucleocapsid proteins (N-protein) exist in the blood,[19] saliva,[20] serum,[21] and nasopharyngeal (NP) swab samples of infected patients[22] and proved to be the most predictive with less susceptibility to mutation for COVID-19 detection in the early phase of infection.[23] It has been used as a reliable disease indicator when used for Rapid Antigen Testing[24] along with the incorporation of Artificial Intelligence and the Internet of Things can provide big data and predictive models for pandemic management.[25−27]

Electrochemical immuno-biosensors have offered ultra-sensitivity as opposed to optical detection methods for clinical detection of various protein biomarkers in different diseases;[28,29] thanks to the use of label-free approaches and employment of conductive nanostructures.[30,31] They have demonstrated their benefits for rapid and sensitive diagnosis of different viral infectious diseases.[32] They have also been used for detection of SARS-CoV-2 RNA and antigen biomarkers,[33,34] with a low limit of detection (LoD) suitable for early disease diagnosis,[35] as well as multiplex detection through multichannel screen-printed electrodes for simultaneous sensing of several biomarkers.[9] Different electrochemical N-protein biosensors such as molecularly imprinted polymer (MIP)-based electrochemical sensors,[36] square wave voltammetric sensing on carbon nanofiber-modified electrodes,[37] and magnetic bead-assisted voltammetry electrochemical assays[20] showed their success for COVID-19 detection.[21,38,39]

Nanomaterials are considered as an inseparable component in the initial phase of fabricating highly sensitive electrochemical biosensors. Zinc oxide (ZnO), carbon nanotubes

Received: December 17, 2021
Accepted: February 9, 2022
Published: February 17, 2022

(CNTs), graphene (Gr),[40,41] and gold nanoparticles (AuNPs)[42] have been introduced as "elite" materials, offering enhancing sensitivity for electrochemical sensing.[43−45] Various forms of ZnO have been used for electrochemical biosensing;[46−48] thanks to their unique properties for creating active sites with a large surface area as well as owning to their high isoelectric point (IEP) of 9.5 contributing to the absorption of biological components such as proteins.[46,49] Being an attractive material for electrochemical biosensor fabrication,[50] graphene[39,51,52] has also been utilized prevalently as a companion element with ZnO in sensing devices,[53−55] for example, for enzymatic[56] and nonenzymatic detection of glucose,[57,58] endorphins,[59] and ascorbic acid.[60] It is worth noting that the coexistence of the graphene and ZnO assists the uniform dispersion of the ZnO NPs inside the mixture.[61] In this study, we get to benefit from these two nanomaterials for developing a ZnO/Gr-based nanocomposite and using it for the detection of SARS-CoV-2 N-proteins. The process involves dispersing the ZnO and reduced graphene oxide (rGO) nanostructures in a buffer solution containing salt ions and coating the sensor with the nanomixture using a single-step nanocoating process without the need for synthesizing the ZnO NPs on rGO. The effect of ionic compounds of the mixture with equal positive and negative charges, obtained from the dissolving of the salts to form a water-based buffer, is investigated to assess uniform dispersion of the nanostructures, leading to the formation of a stable and uniform coating.[62]

Several approaches have been examined for immobilizing bioreceptors on ZnO-contained electrodes. Physical adsorption was tested for immobilizing antibodies on ZnO for immunosensing of human salivary cortisol[63] and α-amylase.[64] Also, carboxyl functional groups existing on graphene[65] form covalent amide bonding with the amine group of antibodies upon their surface deposition, creating more stable bonds and increasing the stability and sensitivity of the immunosensors. To this end, the accompanying elements such as gold nanoparticles have been used to hybridize DNA probe strands[66] on ZnO−Gr nanocomposites to connect the cross-linkers needed for immobilizing the carboxylic groups. In another study, for creating hydrogen peroxide sensors, pyrene succinimide ester (PSE) was utilized to functionalize ZnO−Gr nanocomposites to immobilize streptavidin.[67] A similar functionalization approach was used to create a genosensor detecting coconut cadang−cadang viroid (CCCVd) RNA sequence.[68] The PSE cross-linker, according to its chemical structure, lays within the graphene nanosheets, leaving the functionalization potential of embedded ZnO unleveraged. Only carboxyl groups of the reduced graphene oxide (rGO) were activated using *N*-hydroxysuccinimide-1-ethyl-3-(3-dimethylaminopropyl)carbodiimide (NHS-EDC).[69] (3-Aminopropyl)triethoxysilane (APTES) was also deployed to functionalize ZnO nanorods, enriching the surface with amine groups for antibody immobilization,[70] used for sensing of human serum albumin on a field-effect transistor (FET) immunosensor. The APTES cross-linker was also used in conjunction with glutaraldehyde (GA) activation, for conjugating Aflatoxin B1 target receptors on polyacrylonitrile/ZnO nanofibers in a photoluminescence label-free immunosensor.[71] Despite the effort for successful cross-linking of ZnO essential for sensitive biosensing, the combination of cross-linked ZnO/rGrO for fabricating highly stable electrochemical immunosensors has not yet been explored. Thiol-based L-cysteine cross-linker is a promising cross-linker for creating biosensors,[72] owing to its ability to create stable and strong covalently bonded functional moieties via room-temperature incubation, as opposed to APTES cross-linkers and NHS-EDC activations that often require temperature consideration for their functionalization process.[73]

In this study, for the first time, a self-assemble L-cysteine cross-linker is utilized to enhance the functionality and sensitivity of buffer-based (bb) ZnO/rGO nanocomposites on carbon screen-printed electrodes (cSPEs) for ultrasensitive detection of N-protein in spiked samples and NP swab samples of COVID-19 infected patients. Using electrochemical impedance spectroscopy (EIS), the prepared N-protein immuno-biosensor successfully recognized N-protein within a linear range of 1−10 000 pg/mL, spiked in phosphate-buffered saline (PBS) with a limit of detection (LoD) down to 21 fg/mL and sensitivity of 32.07 ohms·mL/pg·mm^2. Further, positive NP swab samples were distinguished from negative controls by the EIS signals recorded, confirming the utility of this biosensor for clinical detection of COVID-19 infected patients.

2. EXPERIMENTAL SECTION

2.1. Preparation of ZnO-rGO-Coated Electrodes. DS-110 carbon electrodes with carbon as the counter electrode and silver as the reference electrode were purchased (DropSens). A 10 mg/mL solution of rGO nanosheets (Sigma-Aldrich, #910406) was prepared in the water. ZnO nanoparticles, with particle sizes of less than 100 nm dispersed in APTES, were obtained from Sigma-Aldrich (#721077, Sigma-Aldrich). A solution containing 2.5% (v/v) rGO and 2.5% (v/v) ZnO dispersion was prepared in 1× phosphate-buffered saline (PBS) (Growcells, CA, pH = 7.4), given its relatively high concentration of ions (137 mM NaCl, 10 mM phosphate, 2.7 mM KCl) for creating desired charge distribution across the matrix for uniform dispersion of the nanostructures. Ten microliters of this solution was deposited on top of each carbon working electrode using drop casting. After 6 h, the electrodes were rinsed five times in deionized (DI) water to remove PBS salts. The electrodes were incubated overnight at room temperature to allow for stable nanocomposite deposition on the electrode surface. Sodium chloride (NaCl) (#S988, Sigma-Aldrich) and potassium chloride (KCl) (#P3911, Sigma-Aldrich) were dissolved in deionized (DI) water to prepare the matrix used for testing various salt solutions for dispersing the ZnO/rGO nanocomponents.

2.2. Preparation of the N-protein Immuno-Biosensor. bbZnO/rGO-deposited electrodes were drop-casted with 10 mM L-cysteine 97% cross-linker (#168149, Sigma-Aldrich) prepared in DI water. These electrodes were then incubated at room temperature for 4 h to introduce amine and carboxylic functional groups through the formation of a self-assembled monolayer attached to ZnO nanoparticles. Following the washing of functionalized electrodes, N-protein antibodies (anti-N-protein) (HC2003, GenScript Inc.) were diluted in PBS to reach the optimal concentration of 50 μg/mL and deposited on the surface of working electrodes, incubated at room temperature for 1 h, followed by incubation overnight at 4 °C. The antibody (Ab)-immobilized electrodes were rinsed the next day prior to the deposition of 0.1% (w/v) bovine serum albumin (BSA) (#A2153, Sigma). BSA as the blocker agent was dissolved in 1× PBS and incubated on the functionalized electrodes for 15 min at room temperature to eliminate nonspecific binding. SARS-CoV-2 N-protein (GenScript Inc., #Z03488) was used as the target antigen. Standard concentrations of this antigen were prepared in PBS, drop-casted on the surface of the prepared immuno-biosensor, and incubated at room temperature for an optimized interaction time of 15 min before reading the electrochemical signals.

2.3. Characterizations of the Coated Electrode. To assess successful functionalization of the electrodes in different preparation steps, Fourier-transform infrared (FTIR) spectroscopy technique was

https://doi.org/10.1021/acsami.1c24475
ACS Appl. Mater. Interfaces 2022, 14, 10844−10855

carried out using a Bruker IFS 55 Equinox instrument equipped with an MCT cryodetector. Field emission scanning electron microscopy (FESEM, Sigma ZEISS, Germany) was conducted on each electrode to characterize the morphology of the coated materials. An electron beam was swept across the desired area of the electrode where the topography of the coated electrode was observed. A confocal Raman microscope (Alpha 300 R-WiTec) with a laser at 532 nm wavenumber and 60 s accumulation time was utilized to obtain the Raman spectra of the prepared electrodes. Atomic force microscopy (AFM) images in a dynamic force mode (tapping) were obtained (Bruker AFM, Dimension Edge System, Germany) using silicon nitride tips to record and characterize two- and three-dimensional images, histograms, cross sections of the surface images, and surface roughness.

2.4. Electrochemical Characterizations of N-protein Immuno-Biosensors. A PGSTAT 204 potentiostat/galvanostat (Metrohm) was utilized for reading out the electrochemical signals from the electrodes at their different stages of functionalization. All electrochemical tests were performed using the redox probe containing 2.5 mM potassium ferricyanide (III) (#702587, Sigma) and potassium hexacyanoferrate (II) trihydrate (#33358, Alfa Aesar, Thermo Fisher Scientific) dissolved in PBS. For signal measurements, 140 μL of redox solution was drop-casted on cSPEs, covering all three electrodes. The EIS measurement was conducted within a frequency range of 5000−1 Hz, with a single sinus wave (signal amplitude of 10 mV) and the open-circuit potential (E_{ocp}) of 170 mV. The equivalent electrical circuit was fitted and simulated using NOVA 1.11 (Autolab).

2.5. Selectivity Assessment and NP Swab Testing of COVID-19 Infected Patients. To perform cross-reactivity tests, immunoglobulin G (IgG) from the human serum (Sigma; #I4506) and SARS-CoV-2 Spike protein (S1) (Genscript Inc.; #T80202) was purchased. After immobilizing the surface of bbZnO/rGO/L-cysteine-functionalized cSPEs with anti-N-protein and blocking it with BSA, 1 pg/mL each of IgG and S1 proteins, prepared in PBS, was cast-coated on the immuno-biosensor. Another PBS solution containing both 1 pg/mL S1 proteins and 1 pg/mL N-proteins was incubated on the biosensor for 15 min. Following the washing step, the EIS signals were extracted using the previously mentioned parameters. NP swab samples positive or negative for SARS-CoV-2 were obtained from the Alberta Public Health Laboratory (Alberta Precision Laboratories, Calgary, AB). The samples were initially collected in universal/viral transport media for clinical diagnosis of COVID-19 and frozen at −20 °C after testing with real-time quantitative reverse transcription PCR (qRT-PCR). All positive SARS-CoV-2 samples were identified as the Alpha variant of concern (B.1.1.7 lineage). The clinical sample testing was performed in a Biocontainment Level Class II laboratory at the University of Calgary (Ethics ID: REB20-1032), without any prior heat treatment, deactivation, or other sample preparation steps.

3. RESULTS AND DISCUSSION

The biosensor developed in this work benefits from ZnO nanoparticles with improved features of adsorbing of antibodies and stable covalent bonding with the thiolated self-assemble monolayer L-cysteine, along with the enhanced receptor conjugation due to functional groups on the rGO. Scheme 1 represents stepwise modifications of fabricating the bbZnO/rGO-decorated N-protein immuno-biosensor. In short, the bare cSPE is first deposited with a nanodispersion of bbZnO/rGO in PBS, carboxylated after incubation with L-cysteine, and ultimately immobilized with N-protein antibodies. BSA then blocks nonspecific binding sites, preparing the immuno-biosensor for the detection of SARS-CoV-2 N-proteins. The fabricated immunosensor is then linked to the readout system, generating the resulting electrochemical signals associated with the presence of the virus on the surface.

3.1. Physical and Chemical Characterizations of the bbZnO-rGO-Based Nanocomposite. To characterize the deposition of ZnO nanoparticles and rGO nanosheets on the electrode surface, the morphology of the nanocoating was captured using FESEM. ZnO nanoparticles are normally found within the thickness range of 40−100 nm and a semispherical shape, with nanocrystallites packed in each individual aggregate.[74] Graphene nanosheets, on the other hand, are cloth-like transparent structures with single-atom thickness and up to 1 micrometer in width.[75] Figure 1A-a confirms the presence of graphene nanosheets when added to the ZnO dispersion. Graphene nanosheets are located among the ZnO nanoparticles, with a vertical cloth-like sheet that is seen opaque due to the FESEM gold-coating pre-treatment requirement. ZnO nanoparticles are also observed with less than 100 nm in size (an average of 40 nm) and their spherical shape. The antibody immobilization was assessed using the FESEM images, where the surface change upon deposition of antibodies is illustrated in Figure 1A-b. The highlighted areas depict the surface valleys covered with the coated antibody.

Surface topography analysis of ZnO/rGO and ZnO/rGO/Ab coatings was characterized using AFM tapping mode. The rGO nanosheets are uniformly distributed in the ZnO matrix and provide a smooth surface across the films (Figure 1B). The

Scheme 1. Graphical Illustration of the Step-by-Step Immuno-Biosensor Preparation[a]

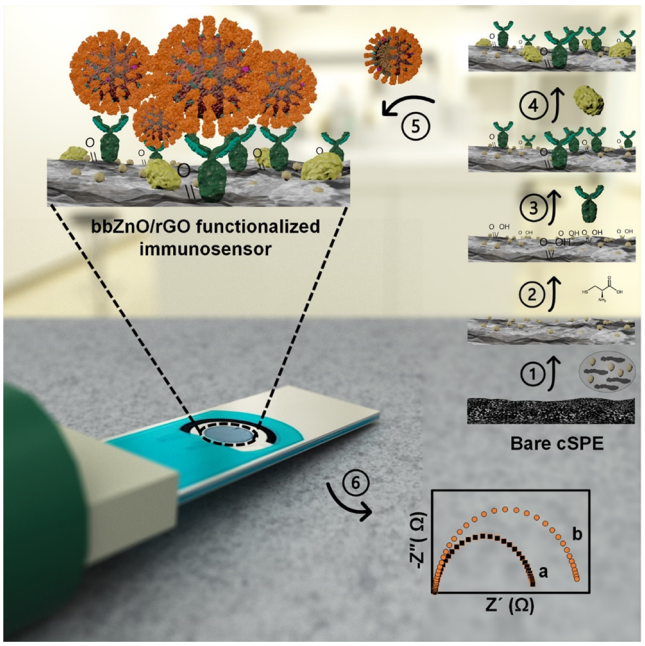

[a]The stepwise sensor preparation is represented through (1) the addition of buffer-based (bb) zinc oxide (ZnO) nanoparticles (illustrated as gray particles) and reduced graphene oxide (rGO) (illustrated as black sheets) on the surface of the bare carbon screen-printed electrode (cSPE), (2) L-cysteine functionalization (the chemical structure of the L-cysteine depicts the existence of thiol and carboxyl functional groups), (3) antibody conjugation (antibody representation in green, the surface is pre-modified with carboxyl functional groups in this step), (4) bovine serum albumin (BSA) deposition (depicted in light green protein clump placed among the antibodies on void areas), and ultimately (5) detection of N-proteins antigens (illustrated by the virus here). (6) The fabricated immunosensor is then connected to the potentiostat for measuring the electrochemical signal from the surface, before (a) and after (b) antigen detection as represented by the Nyquist plot showing the electrochemical impedance spectroscopy (EIS) results.

https://doi.org/10.1021/acsami.1c24475
ACS Appl. Mater. Interfaces 2022, 14, 10844−10855

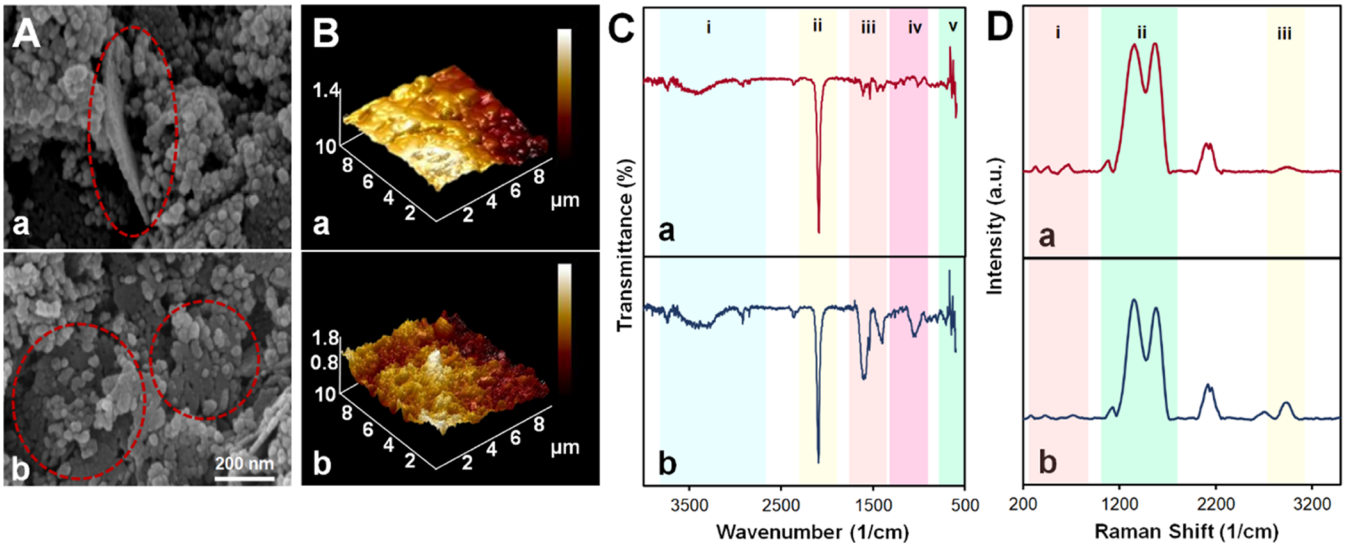

Figure 1. Physical and chemical characterizations of ZnO-rGO-coated electrodes. (A) Field emission scanning electron microscopy (FESEM) obtained from (a) surface of the ZnO/rGO composition coated on cSPE with both graphene nanosheets and ZnO nanoparticles visible and (b) same surface in (a) where deposited with antibodies (scale bar: 200 nm). (B) Images obtained from atomic force microscopy (AFM), representing the roughness of (a) ZnO/rGO-modified electrode and (b) same surface coated with antibodies for the surface area of 10 × 10 μm^2. (C) Attenuated total reflectance (ATR) mode of Fourier-transform infrared spectroscopy (FTIR) and (D) Raman spectroscopy graphs for chemical analysis of (a) bbZnO/rGO coating and (b) L-cysteine-functionalized bbZnO/rGO coating.

average values of root-mean-square (RMS) roughness (R_q) for the ZnO/rGO and ZnO/rGO/Ab coatings are 222 and 199 nm, respectively. The ZnO/rGO/Ab coating has a smoother surface compared to the ZnO/rGO coating, attributed to Abs filling the voids and making a smoother surface (comparing Figure 1B-a,b). The AFM height histograms of ZnO and ZnO/rGO coatings (Figure S1) also show a high uniformity of the deposited films, measured for the surface area of 10 × 10 μm^2. The height histograms have a normal data dispersion, and the shapes of curves are mostly symmetrical, which indicates the coexistence of hills and wells of identical sizes distributed on the surfaces. The surface functionalized with L-cysteine was also analyzed using FESEM and AFM, with no significant changes observed as opposed to the ZnO/rGO-coated surface, owing to the molecular scale coating on the surface (Figure S2).

The ATR spectroscopy, as a mode of FTIR spectroscopy, was conducted to perform functional analysis on the coating, the results of which are shown in Figure 1C. The spectrum of ZnO/rGO shows a band at 1495 cm^{-1} (iii) wavelength due to the skeletal vibration of graphene, in addition to a broad absorption band at 3357 cm^{-1} (i) associated with the stretching vibrations of the hydroxyl groups of water molecules absorbed over the surface of ZnO/rGrO.[76] The existing C−OH and COO− bonds of 3430 cm^{-1} (i) and 2360 cm^{-1} (ii), respectively, were found in the spectrum, which are rooted in the porosity and hygroscopic nature of graphene. The characteristic bonds at 1440, 1390, and 1230 cm^{-1} (iii) were attributed to C−H stretching, C−O stretching, and C−O vibration, correspondingly. Also, the peaks of S−O bonds were represented at 972−1010 cm^{-1} (iv) wavelengths, in both spectra, with a higher intensity in the ZnO/rGO/L-cysteine spectra (Figure 1C-b). Furthermore, the ATR spectrum was able to reveal the board O−H stretching vibration [3230−3554 cm^{-1} (i)], C═O stretching vibration [1720−1750 cm^{-1} (iii)], and associated Zn−O [597−704 cm^{-1} (v)] functional groups.[55,77,78] Through this analysis, the C═C peak from unoxidized sp^2 C−C bonds was also observed at 1576−1620 cm^{-1} (iii) wavelengths (Figure 1C-a) and with higher intensity in the ZnO/rG/L-cysteine (Figure 1C-b). The spectrum of L-cysteine (Figure 1C-b) was labeled as a (−NH) bending vibration at 1263 cm^{-1} (iv), along with the peaks around 900 cm^{-1} (iv), proving the existence of the −COOH functional group. The sharp peak of the C═O bond in both ZnO/rGO and ZnO/rGO/L-cysteine coatings was indicated at 2100 cm^{-1} (ii).[79]

Raman spectroscopy was carried out to analyze surface-specific vibrational states of ZnO/rGO and ZnO/rGO/L-cysteine coatings. The Raman spectrum illustrates two characteristic peaks situated at 1315 and 1595 cm^{-1} (ii), which are assigned as D and G peaks, respectively (Figure 1D-a). The D peak is related to the breathing mode of *k* point phonons of A_{1_g} symmetry, arising owing to local defects and disorders, particularly at the edges of graphene. The G peak, on the other hand, is ascribed to the A_{2_g} phonon mode of sp^2-hybridized carbon atoms presented within the graphene matrix.[80] The Raman shift of ZnO was observed at 373 cm^{-1} (i), generated from the second-order Raman spectrum arising from zone boundary phonons of the hexagonal ZnO. The peak appeared at 445 cm^{-1} (i) is attributed to the nonpolar optical phonon E_2 high-frequency mode of ZnO in the wurtzite structure from the C_{6v} symmetry group.[81,82] This confirms that hexagonal wurtzite ZnO crystallites are formed on the graphene layer. The peak at 620 cm^{-1} (i) corresponds to the E1 (LO) mode of hexagonal ZnO, which is associated with oxygen deficiencies.[81,83] The multiple phonon scattering is also observed at 1126 cm^{-1} (ii).[84] The Raman spectrum of the ZnO/rGO/L-cysteine film (Figure 1D-b) illustrates similar characteristic peaks of ZnO as well as G and D bands of ZnO/rGO. The intensity ratios of D and G peaks (I_D/I_G) in ZnO/rGO and ZnO/rGO/L-cysteine were determined to be 0.98 and 1.02, respectively. It is known that ZnO/rGO is a highly defective structure in which I_D/I_G decreases as an increasing

https://doi.org/10.1021/acsami.1c24475
ACS Appl. Mater. Interfaces 2022, 14, 10844−10855

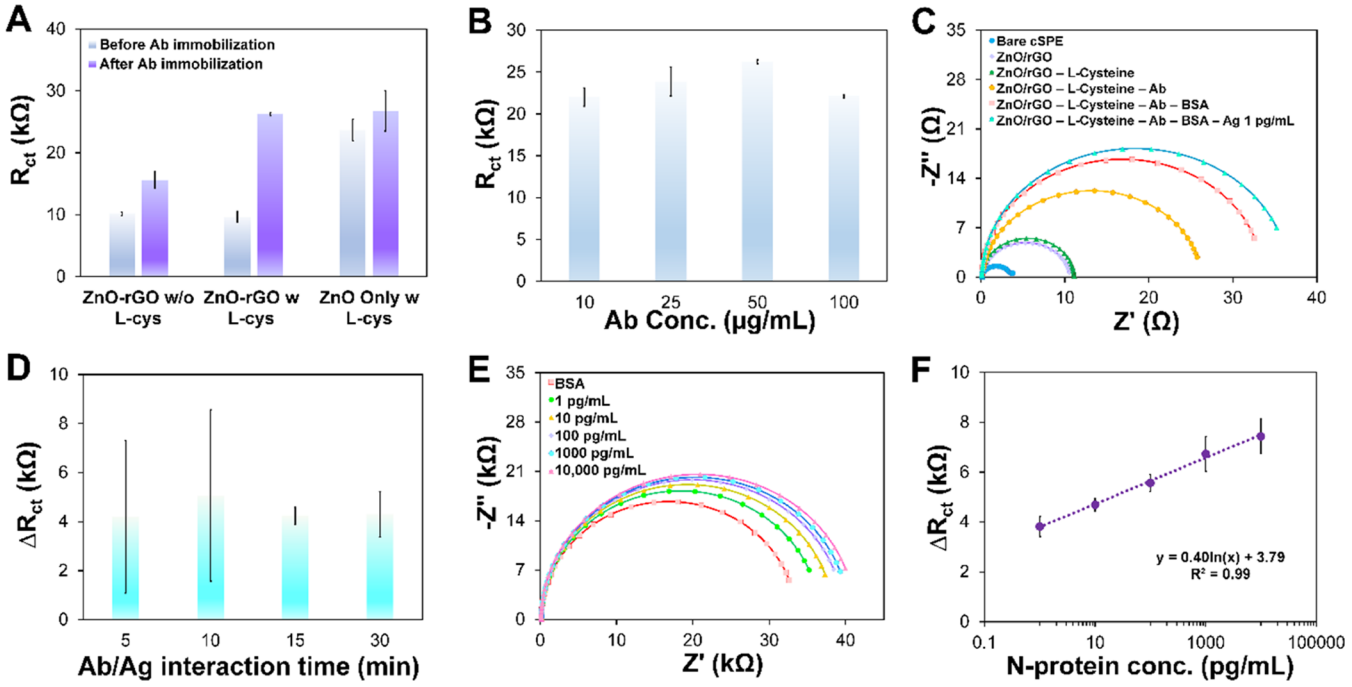

Figure 2. Electrochemical characterizations of the bbZnO/rGO N-protein immuno-biosensor. (A) Charge-transfer signals for different compositions of nanocoating [2.5% (v/v) ZnO only, bbZnO/rGO composite, and L-cysteine self-assembled monolayer cross-linked surface on the ZnO/rGO] before and after immobilization of the 50 μg/mL N-protein antibody on the working electrode. (B) EIS signal of the immunosensor in response to various tested concentrations of the antibody (10, 25, 50, and 100 μg/mL) was used to find the optimal antibody concentration. (C) Nyquist plots representing the stepwise deposition of nanocoating, L-cysteine cross-linker, nucleocapsid antibody, bovine serum albumin (BSA) blocker, and 1 pg/mL nucleocapsid target protein (antigen). (D) Charge-transfer resistance signals obtained for different incubation times (5, 10, 15, 30 min) were used to obtain the optimal (minimal) interaction time needed to ascertain the completion of the antibody−antigen interaction. (E) Nyquist diagrams obtained from electrochemical impedance spectroscopy (EIS) measurements of the immuno-biosensor subject to standard concentrations of N-protein prepared in PBS and (F) corresponding calibration curve of the biosensor.

defect density. Furthermore, the G peak in the ZnO/rGO/L-cysteine film is slightly red-shifted by 8 cm^{-1} compared to the ZnO/rGO film. The deviation of the G peak corresponds to the functionalization of organic molecules on the surfaces of carbon layers,[85] confirming that L-cysteine molecules are functionalized on the surface of the rGO layer. Raman spectroscopy was utilized to investigate the single-, bi-, and multilayer characteristics of rGO layers, with the 2D peak of the single-layer graphene nanosheet observed at 2878 cm^{-1} (iii).[86]

3.2. Electrochemical Characterizations of bbZnO-rGO-Coated Electrodes. *3.2.1. Compositions of the Coated Nanomaterial.* In this work, the specific characteristics of ZnO nanoparticles and graphene-based nanosheets were employed for the fabrication of highly sensitive and stable immuno-biosensors.[43] First, the addition of the ZnO nanocomponent, more specifically particles with the size of less than 100 nm, increases the effective surface area of the working electrode, where the target analytes are captured, leading to the rise in the sensitivity of the biosensor.[87] The chemical characteristics of this metal oxide are also employed for anchoring thiolated self-assemble monolayers, introducing more carboxyl functional groups to the surface.[43] Second, graphene has been extensively used as one of the carbon-based nanostructures for fabricating nanobiosensors due to its biocompatibility,[88] nontoxicity,[89] and excellent electrical properties.[90] rGO nanosheets added to the ZnO-coated surface add more carboxyl functional groups to the surface of the electrode. The rGO nanomaterial is known to be compatible with ZnO nanoparticles and has been previously used for supporting the ZnO nanoparticles and preserving the stability of the nanocomposite.[56] Hence, the combined ZnO-rGO composite has the potential in providing an abundant source of functional moieties on the surface of the working electrode required for antibody immobilization. Here, we showed the need for combining these nanostructures to achieve a stable coating while providing a high affinity for antibody optimization needed for fabricating an ultrasensitive immunosensor. To this end, this nanocomposite, with defined volume concentrations, was mixed into a base solution and deposited and dried on the electrode surface to be further used for biosensing.

The uniform dispersion of the ZnO/rGO nanocomponents was assessed when mixed into various salt-based solutions, including 1× PBS, 2.5 mM NaCl in water, and 2.5 mM KCl in water (Table S1). Owing to the initial suspension of both graphene and ZnO dispersions in water and considering the polarity of ZnO, the selected ion-enriched solutions are suitable matrices for the dispersion of this nanocomposite.[62] The stability of the nanomaterial coated on the surface of cSPEs was evaluated applying 10 cycles of the potential by the cyclic voltammetry (CV) technique. After coating the electrodes with each of the mixed dispersions, the coated electrodes were rinsed, dried, and underwent CV measurements, within the potential window of −0.4 to 1 V in a 2.5 mM $[Fe(CN)_6]^{3-/4-}$ redox probe in PBS (Figure S3). Comparing the voltammograms confirms the contribution of rGO to the stability of the nanocomposite coating, where a considerable current drop in the consecutive cycles of applied potential is observed for the only ZnO coating [2.5% (v/v) ZnO dispersed in PBS; the redox solution of $K_3(Fe(CN)_6)/K_4(Fe(CN)_6)$]

https://doi.org/10.1021/acsami.1c24475
ACS Appl. Mater. Interfaces 2022, 14, 10844−10855

(Figure S3A,B). It is noted that surface stability did not improve even adding rGO [2.5% (v/v)] to the ZnO suspension made in 2.5 mM KCl (Figure S3C) and 2.5 mM NaCl (Figure S3D). Alternatively, PBS was tested as the dispersion matrix, with a dispersed 1% (v/v) ZnO and rGO (Figure S3E) and 2.5% (v/v) ZnO and rGO (Figure S3F), wherein the latter showed the highest surface stability, with lowest peak current drop of 0.81% from the second oxidation peak current to the last oxidation peak current in the CV cycles. The differential peak currents between the second and the last oxidation cycles were measured for other surfaces and are presented in Table S1. The results depict that high concentrations of the ionic compounds in PBS (137 mM NaCl, 10 mM phosphate, 2.7 mM KCl) are effective in creating the charge distribution required for uniform dispersion of the polar ZnO nanoparticles.[62] Also, the existence of the electrical charges on the rGO enhances its uniform dispersion in polar/ionic solvents (e.g., water or PBS).[91] The highly stable surface coating (2.5% (v/v) ZnO and rGO in PBS) was used for proceeding with longitudinal stability analysis of the coated electrodes, with CV measurements performed 7, 21, and 30 days following the initial nanomaterial coating. While all of the electrodes were stable for biosensing during a 1-month period, a slight drop in the peak current is observed comparing the results of electrodes tested on different days (moving from day 1 to day 7 (7.5% reduction) and day 1 to day 30 (12.5% reduction)) (Figure S4). This drop in the peak signal needs to be considered for the use of different batches of electrodes depending on their shelf-life coating. It is noted that all biosensing data presented in this work are for freshly coated electrodes, unless otherwise mentioned.

A solution of the 2.5 mM $[Fe(CN)_6]^{3-/4-}$ redox probe in PBS was used for conducting all electrochemical measurements and investigating the electrochemical reaction mechanism on the surface of working electrodes, coated with the selected nanocomposite, i.e., 2.5% (v/v) of ZnO and rGO in PBS. In this regard, CV measurements were performed with scan rates ranging from 10 to 700 mV/s (Figure S5A). The correlation of reduction and oxidation peak currents with the scan rate (adsorption) and the square root of the scan rate (diffusion) is shown in Figure S5B,C, respectively. As illustrated, the linear correlation is found within the current versus square root of the scan rate, showing the diffusion-control mechanism of reduction/oxidation reactions.

To evaluate whether carboxyl moieties contribute to the level of antibodies captured on the electrodes, first, the Ab-immobilized bbZnO/rGo-coated electrodes were subject to EIS measurement in the absence of the cross-linker L-cysteine (Figure 2A). The EIS signals show that the existence of the intrinsic carboxylic groups in the rGO nanosheets along with the electrical characteristic of ZnO nanoparticles for bioanalyte adsorption increases the charge-transfer resistance (R_{ct}) signals from 10.14 ± 0.31 kΩ for Ab-free biosensors to 15.60 ± 1.37 kΩ for antibody-deposited electrodes. This verifies the immobilization of antibody bioreceptors on the surface (ΔR_{ct} = 5.45 kΩ) in the absence of the cross-linker.

To further assess the contribution of the cross-linker in antibody immobilization, the bbZnO/rGo-coated electrodes were functionalized with 10 mM L-cysteine solution, forming a self-assembled monolayer containing carboxyl functional groups. Following the immobilization of Ab on bbZnO/rGo/L-cysteine electrodes, the R_{ct} signal changed from 9.60 ± 0.88 kΩ for the pre-Ab-immobilized electrode to 26.23 ± 0.23 kΩ for the Ab-immobilized electrode (ΔR_{ct} = 16.63 kΩ). This significant change in R_{ct} indicates the effective role of L-cysteine in enhancing the surface potential for antibody capturing and hence increasing the sensitivity of the biosensor. Comparing the R_{ct} for the biosensors functionalized with L-cysteine (16.63 kΩ) as opposed to those of bbZnO/rGO-non-functionalized biosensors (5.45 kΩ) shows that L-cysteine functionalization increases conjugation of antibodies on the working electrode.

Also, another group of electrodes was coated with 2.5% (v/v) ZnO in PBS (without any rGO) to showcase the role of rGO not only in adding stability to the biosensor but also in enhancing the surface capacity for antibody immobilization. The results show that elimination of conductive rGO increases surface charge resistance and decreases ΔR_{ct} (3.06 ± 3.23 kΩ), demonstrating a decline in surface capacity in antibody immobilization in the absence of rGO. Ultimately, the optimal antibody concentration was determined to be 50 pg/mL, upon evaluating the R_{ct} signals for 10, 25, 50, and 100 pg/mL antibody concentrations spiked in PBS (Figure 2B). The associated Nyquist plots for the antibody optimization process are shown in Figure S6A.

3.3. Detection Performance of the N-protein Immuno-Biosensor. The formation of semicircles in the Nyquist plots obtained from EIS measurements reveals the electrochemical characteristics of the electrode surface and the associated electrical fit with its simulated equivalent circuit ($[R_s(R_{ct}Q)]$). In this equation, R_s is the solution resistance, R_{ct} is the charge-transfer resistance, and Q is the constant phase element (CPE). Figure 2C depicts the Nyquist plot corresponding to the bbZnO-rGO nanocomposite coated on the electrode surface as opposed to the bare cSPE. The increase in R_{ct} from 1.72 ± 0.21 kΩ for the bare cSPE to 10.14 ± 1.73 kΩ for the bbZnO/rGo-coated electrode confirms electrochemically the formation of the coating layer on the electrode surface. The coated electrodes were reproducible, showing an relative standard deviation (RSD) of 3.06% in the signals measured by EIS for three different electrodes. The R_{ct} values reported here are associated with the mean of three replications; however, the plot in Figure 2C only depicts the Nyquist plot for one of the measurements. The formation of the complete semicircle in the Nyquist plot indicates that the coating has not adversely affected the electrochemical properties of the surface. Also, the increase in the R_{ct} value confirms stable deposition of the coating layer, with ZnO as a semiconductor material hindering the path for charge transfer. Furthermore, functionalizing the surface of the bbZnO/rGO-coated electrode with L-cysteine molecules causes a minimal change in the R_{ct} values (5.32%, R_{ct} changes from 10.14 ± 1.73 kΩ for the bbZnO/rGO-coated electrode to 9.60 ± 0.88 kΩ for the L-cysteine-functionalized electrode). Finally, the successful conjugation of antibodies on the surface of the functionalized electrode is detectable via the increase in R_{ct} (173.16% increase in R_{ct}, with the R_{ct} = 26.23 ± 0.23 kΩ for antibody-immobilized electrodes). This confirms the existence of an increased amount of carboxylic functional groups (due to the addition of graphene and L-cysteine) and forming covalent amidic bonds with the amine functional groups of the antibody. Adding the blocking agent (here BSA) to the Ab-coated electrode further increases R_{ct} (27.20% increase in R_{ct} reaching to 33.36 ± 0.45 kΩ for the BSA-coated electrodes) and completes the process of creating the N-protein immuno-

https://doi.org/10.1021/acsami.1c24475
ACS Appl. Mater. Interfaces 2022, 14, 10844−10855

biosensor. Exposing the immuno-biosensor to the 1 pg/mL N-protein antigen (spiked in PBS) and washing it with the DI water for removing nonspecific bindings completes the immunoreaction, resulting in a rise in the radius of the Nyquist plot's semicircle (an increase of 11.48% in R_{ct} reaching to 37.17 ± 0.40 kΩ). The BSA concentration was also optimized to reduce the background signal, allowing for detecting the biomarker in a wide detection range, with the Nyquist plots of different BSA concentrations [0.001, 0.01, 0.1, 1% (w/v)] and the associated R_{ct} measurements presented in Figure S6C,D.

To investigate the performance of the N-protein immuno-biosensor, solution samples containing defined concentrations (0.5, 1, 10, 100, 1000, and 10 000 pg/mL) of N-proteins were prepared by a serial dilution of the stock N-protein into PBS. Optimizing the antibody−antigen immunoreaction time showed that a minimal interaction time of 15 min is needed (Figure 2D), which is considered a rapid immunoreaction response essential for developing rapid biosensing testing kits. EIS measurements were conducted to obtain electron-transfer resistance signals for recognizing N-protein with increasing concentrations. The results show that the radius of the Nyquist semicircle increased, for example, from 32.6 kΩ for zero concentration of N-protein to 35.2 kΩ for 1 pg/mL N-protein and 40 kΩ for 10 ng/mL N-protein concentration as the highest tested concentration (Figure 2E). The corresponding calibration curve is plotted in Figure 2F, wherein the overall sensitivity of 32.07 ohms·mL/pg·mm^2 and a limit of detection (LoD) of 0.02 pg/mL are obtained for the detection of N-proteins. The linear detection range for the N-protein immuno-biosensor was found to be 1 pg/mL to 10 ng/mL, with the limit of quantification (LOQ) of 14.9 pg/mL. The reliability and accuracy of the presented immunosensor are presented by noticing no or minimal overlap between the error bars of different measured concentrations of the N-protein antigen within the calibration curve. Given the need for COVID-19 rapid tests with the lowest possible LoD for detecting samples with low viral loads while maintaining a wide dynamic detection range, the superiority of our N-protein immuno-biosensor over the previously developed N-protein immunosensors is demonstrated in a comparative evaluation presented in Table 1. Exploring this table, our immunosensor combines both rapid detection and a very low limit of detection (in fg/mL level), needed for early diagnosis of SARS-CoV-2. It is worth noting that the level of complexity in the fabrication process of our work was comparable or less than the other methods.

The selective response of the bbZnO/rGrO immuno-biosensor was first assessed through cast coating of human immunoglobulin G (IgG) and human SARS-CoV-2 spiked (S1) proteins on the biosensors. The rationale for this selection is related to the coexistence of IgG and S1 proteins (on the surface of the virus or freely available in the sample) along with N-proteins existing in clinical samples of infected individuals.[94,95] The immuno-biosensor was incubated with different solutions, including only 1 pg/mL IgG, only 1 pg/mL S1 protein, and 1 pg/mL both of S1 and N-proteins (Figure 3A). The results of specificity testing show that the R_{ct} signals for testing the biosensors with spiked samples containing IgG and S1 proteins (0.21 ± 0.07 and 0.91 ± 0.72 kΩ, respectively) are significantly lower than the response of the biosensor tested with 1 pg/mL N-protein spiked samples (3.81 ± 0.40 kΩ; P-value < 0.05). Also, an insignificant difference between the R_{ct}

Table 1. Electrochemical Immuno-Biosensors Developed for Detection of SARS-CoV-2 Nucleocapsid Protein Antigens

surface chemistry	electrochemical method	limit of detection (LoD)	linear detection range	clinical sample validation	time of detection	biofluid tested	sensitivity	ref
poly-*m*-phenylenediamine (PmPD), molecularly imprinted polymer	DPV[a]	0.7 pg/mL	0.9−5.2 pg/mL	yes	30 min	lysis buffer (LB)	not reported	36
carboxylated magnetic nanobeads on the gold screen-printed electrode	CA[b]	50 pg/mL	0.1−10 000 pg/mL	yes	50 min	serum	not reported	21
laser-engraved graphene (LEG) cross-linked with 1-pyrenebutyric acid	DPV−EIS[c]	not reported	50−5000 pg/mL	yes	3 h	PBS	not reported	92
carbon nanofiber electrografted with diazonium on carbon screen-printed electrodes	SWV[d]	0.8 pg/mL	1−1000 ng/mL	yes	3 h	PBS	not reported	37
carbon black-based SPE, magnetic bead assisted	DPV	8000 pg/mL in saliva	not reported	yes	30 min	diethanolamine buffer (DEA)	not reported	20
gold nanoparticle functionalized with 11-mercaptoundecanoic acid (MUA) on the carbon screen-printed electrode	SWV	0.4 pg/mL	1 pg/mL to 100 ng/mL	yes	15 min	PBS	not reported	93
L-cysteine-functionalized bbZnO/rGO immunobiosenosr	EIS	21 fg/mL	1−10 000 pg/mL	yes	15 min	PBS	32.07 ohms·mL/pg·mm^2	this study

[a]DPV, differential pulse voltammetry. [b]CA, chronoamperometry. [c]EIS, electrochemical impedance spectroscopy. [d]SWV, square wave voltammetry.

https://doi.org/10.1021/acsami.1c24475
ACS Appl. Mater. Interfaces 2022, 14, 10844−10855

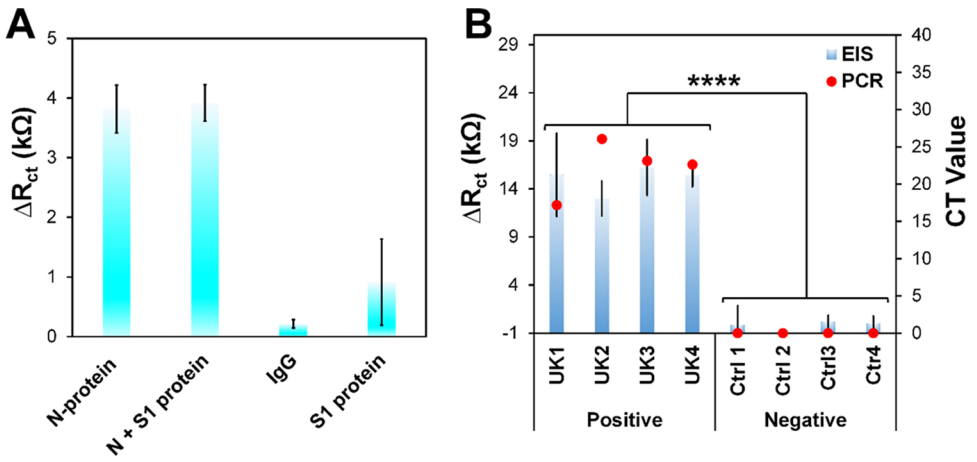

Figure 3. Selectivity and clinical performance of the bbZnO/rGO N-protein immuno-biosensor. (A) Selective EIS response of the immuno-biosensor incubated with 1 pg/mL N-protein and 1 pg/mL S1/N-protein solutions as opposed to 1 pg/mL only human immunoglobulin G (IgG) and SARS-CoV-2 S1 protein spiked in PBS. (B) Charge-transfer resistance signals of the EIS measurements in nasopharyngeal (NP) swab samples of four positive patients and four negative control individuals, along with the CT-values obtained from real-time quantitative reverse transcription-polymerase chain reaction (qRT-PCR) tests (P-value < 0.05).

values of the biosensors tested with N-protein spiked samples and combined S- and N-proteins spiked samples confirms the high specificity of the immuno-biosensor to detect N-proteins in the presence of interferences.

Finally, the functionality of the immuno-biosensor was assessed for differentiating infected patients and controls. Four SARS-CoV-2 positive patients (with viral particles associated with the variant B.1.1.7) and four negative controls were tested with this immuno-biosensor. The samples were collected in universal transport media (UTM) by the Alberta Provincial Laboratory (APL; Calgary, Canada). The samples did not need any step of purification, filtration, thermal treatment, or lysis prior to the experiment, and all tests were performed under Class II Biosafety Cabinet. Each positive and negative sample without any preparation was drop-casted on the immuno-biosensor and incubated for 15 min prior to recording the EIS signals. The successful immunoreaction of N-proteins existing in the NP swab samples of infected patients is confirmed via the significant difference (cut-off value = 3 kΩ, P-value < 0.05) of their EIS signals compared to those obtained from the control group. The clinical samples were already tested by APL using qRT-PCR, CT-values of which are shown in Figure 3B. The performance of the immuno-biosensor for detecting N-proteins in clinical samples was further compared to the Abbott Panbio COVID-19 N-protein Ag Rapid Test Device (Reported Panbio's clinically sensitivity of 82% and specificity of 100%[96]). These commercially available lateral flow assay strips (require 100 μL of the sample) also detect N-proteins in NP swab samples, with a turnaround time of 15 min, although they cannot quantify N-protein concentration. For the small number of clinical samples tested in this work, 100% agreement was achieved for the results obtained from the Panbio test and the bbZnO/rGO immuno-biosensor (Figure S7). Further clinical validation in a larger cohort is needed to compare the clinical sensitivity and specificity of the N-protein immuno-biosensor with the other PoC testing kits (e.g., Abbott Panbio)

4. CONCLUSIONS

The demand for COVID-19 rapid testing continues to grow even after widespread vaccinations. Detecting trace levels of viral antigens, particularly those with minimal risk of mutation (e.g., nucleocapsid protein antigen), have shown to have a diagnostic value comparable to the nucleic acids of the virus. In the present work, the surface of carbon electrodes was modified with a stable nanocomposite containing ZnO nanoparticles accompanied with rGO nanosheets dispersed in a buffer, to enable the most sensitive and selective detection of the SARS-CoV-2 N-protein antigen reported. The results obtained from stability assessments of the coated nanostructure confirm that utilization of ionic salt solution (PBS buffer) as the matrix for preparation of the nanomixture plays a key role in taking advantage of the polarity of ZnO NPs as well as an intrinsic charge of the rGO sheets for yielding a uniform dispersion, forming a stable and uniform sensor nanocoating. The thiol-based self-assembled monolayer of L-cysteine contributed to increasing the efficiency of antibody conjugation and biosensor sensitivity. Among limited electrochemical biosensors reported in the literature for detection of N-proteins, the bbZnO/rGO immuno-biosensor could accomplish yielding acceptable sensitivity and a low limit of detection in spiked samples, which is profoundly significant when it comes to early COVID-19 diagnosis. The initial testing of the N-protein immuno-biosensor was successful for differentiating infected patients from the controls, providing evidence of the appropriateness of the nanocomposite as a reliable biosensor coating. Future works can elaborate on evaluating the clinical performance of this biosensor tested in larger cohorts of COVID-19 infected patients with different variants, detecting other COVID-19 antigen biomarkers (e.g., S1 protein), and multiplex detection of several biomarkers for differentiating different viruses (e.g., SARS-CoV-2 and influenza). For future studies, the clinical sensitivity and specificity of the immunosensor would be evaluated in larger patient cohorts and its sensing steps would be integrated into automated fluid-handling units, enabling the production of sample-to-result rapid testing kits.

■ ASSOCIATED CONTENT

Supporting Information

The Supporting Information is available free of charge at https://pubs.acs.org/doi/10.1021/acsami.1c24475.

https://doi.org/10.1021/acsami.1c24475
ACS Appl. Mater. Interfaces 2022, 14, 10844−10855

List of different compositions for the preparation of ZnO-based nanocoating; AFM 2D images, cross sections, and histograms of the ZnO and ZnO/rGO surface; FESEM and AFM data of the L-cysteine-functionalized ZnO/rGO surface; electrochemical characterization of different compositions of coating materials; shelf-life stability analysis of the bbZnO/rGO-coated surface; electrochemical characterization of the bbZnO/rGo-coated electrodes for determining the diffusion-control mechanism; optimizing the immunobiosensor parameters in terms of antibody and BSA concentrations; the results of testing clinical samples using Panbio COVID-19 Ag Rapid Test Device (PDF)

AUTHOR INFORMATION

Corresponding Author

Amir Sanati-Nezhad − *BioMEMS and Bioinspired Microfluidic Laboratory, Department of Mechanical and Manufacturing Engineering, University of Calgary, Calgary, Alberta T2N 1N4, Canada; Center for BioEngineering Research and Education and Biomedical Engineering Graduate Program, University of Calgary, Calgary, Alberta T2N 1N4, Canada;* orcid.org/0000-0002-2309-2388; Email: amir.sanatinezhad@ucalgary.ca

Authors

Fatemeh Haghayegh − *BioMEMS and Bioinspired Microfluidic Laboratory, Department of Mechanical and Manufacturing Engineering, University of Calgary, Calgary, Alberta T2N 1N4, Canada*

Razieh Salahandish − *BioMEMS and Bioinspired Microfluidic Laboratory, Department of Mechanical and Manufacturing Engineering, University of Calgary, Calgary, Alberta T2N 1N4, Canada; Center for BioEngineering Research and Education, University of Calgary, Calgary, Alberta T2N 1N4, Canada*

Mohsen Hassani − *BioMEMS and Bioinspired Microfluidic Laboratory, Department of Mechanical and Manufacturing Engineering, University of Calgary, Calgary, Alberta T2N 1N4, Canada*

Complete contact information is available at: https://pubs.acs.org/10.1021/acsami.1c24475

Author Contributions

‖F.H. and R.S. contributed equally to this work.

Author Contributions

Concept and design: F.H., R.S.; Experimentation & Data acquisition: F.H., R.S.; Data analysis and/or interpretation: F.H., R.S., M.H., and A.S.-N.; Clinical sample analysis: R.S., F.H.; Drafting and revising the manuscript: F.H., R.S., M.H., and A.S.-N.

Notes

The authors declare no competing financial interest.

ACKNOWLEDGMENTS

The authors acknowledge the Canadian Institutes of Health Research (CIHR) and Natural Sciences and Engineering Research of Canada (NSERC) for their Rapid COVID-19 Response funding. The authors also acknowledge the Canada Research Chair, University of Calgary, and CMC Microsystems, Canada for supporting this research. The authors would also like to thank Calgary ProveLab and their staff members LeeAnn Turnbull and Kanti Pabbaraju for their support in providing access to clinical samples.

REFERENCES

(1) Qin, Z.; Peng, R.; Baravik, I. K.; Liu, X. Fighting COVID-19: Integrated micro-and nanosystems for viral infection diagnostics. *Matter* **2020**, *3*, 625−651.

(2) Valera, E.; Jankelow, A.; Lim, J.; Kindratenko, V.; Ganguli, A.; White, K.; Kumar, J.; Bashir, R. COVID-19 Point-of-Care Diagnostics: Present and Future. *ACS Nano* **2021**, *15*, 7899−7906.

(3) Yüce, M.; Filiztekin, E.; Özkaya, K. G. COVID-19 diagnosis—A review of current methods. *Biosens. Bioelectron.* **2020**, *172*, No. 112752.

(4) Zarubova, J.; Zhang, X.; Hoffman, T.; Hasani-Sadrabadi, M. M.; Li, S. Biomaterial-based immunoengineering to fight COVID-19 and infectious diseases. *Matter* **2021**, *4*, 1528−1554.

(5) Shao, W.; Shurin, M. R.; Wheeler, S. E.; He, X.; Star, A. Rapid Detection of SARS-CoV-2 Antigens Using High-Purity Semiconducting Single-Walled Carbon Nanotube-Based Field-Effect Transistors. *ACS Appl. Mater. Interfaces* **2021**, *13*, 10321−10327.

(6) Dang, Y.; Liu, N.; Tan, C.; Feng, Y.; Yuan, X.; Fan, D.; Peng, Y.; Jin, R.; Guo, Y.; Lou, J. Comparison of qualitative and quantitative analyses of COVID-19 clinical samples. *Clin. Chim. Acta* **2020**, *510*, 613−616.

(7) Kim, H.-s.; Abbas, N.; Shin, S. A rapid diagnosis of SARS-CoV-2 using DNA hydrogel formation on microfluidic pores. *Biosens. Bioelectron.* **2021**, *177*, No. 113005.

(8) Haghayegh, F.; Salahandish, R.; Zare, A.; Nezhad, A. S. Immunobiosensor on a chip: a self-powered microfluidic-based electrochemical biosensing platform for point-of-care quantification of proteins. *Lab Chip* **2021**, *22*, 108−120.

(9) Li, J.; Lin, R.; Yang, Y.; Zhao, R.; Song, S.; Zhou, Y.; Shi, J.; Wang, L.; Song, H.; Hao, R. Multichannel Immunosensor Platform for the Rapid Detection of SARS-CoV-2 and Influenza A (H1N1) Virus. *ACS Appl. Mater. Interfaces* **2021**, *13*, 22262−22270.

(10) Wang, C.; Cheng, X.; Liu, L.; Zhang, X.; Yang, X.; Zheng, S.; Rong, Z.; Wang, S. Ultrasensitive and Simultaneous Detection of Two Specific SARS-CoV-2 Antigens in Human Specimens Using Direct/Enrichment Dual-Mode Fluorescence Lateral Flow Immunoassay. *ACS Appl. Mater. Interfaces* **2021**, *13*, 40342−40353.

(11) Sharma, P. K.; Kim, E.-S.; Mishra, S.; Ganbold, E.; Seong, R.-S.; Kaushik, A. K.; Kim, N.-Y. Ultrasensitive and Reusable Graphene Oxide-Modified Double-Interdigitated Capacitive (DIDC) Sensing Chip for Detecting SARS-CoV-2. *ACS Sens.* **2021**, *6*, 3468−3476.

(12) Derakhshan, M. A.; Amani, A.; Faridi-Majidi, R. State-of-the-Art of Nanodiagnostics and Nanotherapeutics against SARS-CoV-2. *ACS Appl. Mater. Interfaces* **2021**, *13*, 14816−14843.

(13) Wu, K.; Chugh, V. K.; Krishna, V. D.; di Girolamo, A.; Wang, Y. A.; Saha, R.; Liang, S.; Cheeran, M. C.; Wang, J.-P. One-Step, Wash-free, Nanoparticle Clustering-Based Magnetic Particle Spectroscopy Bioassay Method for Detection of SARS-CoV-2 Spike and Nucleocapsid Proteins in the Liquid Phase. *ACS Appl. Mater. Interfaces* **2021**, *13*, 44136−44146.

(14) Ahmadivand, A.; Gerislioglu, B.; Ramezani, Z.; Kaushik, A.; Manickam, P.; Ghoreishi, S. A. Functionalized terahertz plasmonic metasensors: Femtomolar-level detection of SARS-CoV-2 spike proteins. *Biosens. Bioelectron.* **2021**, *177*, No. 112971.

(15) Yamaoka, Y.; Miyakawa, K.; Jeremiah, S. S.; Funabashi, R.; Okudela, K.; Kikuchi, S.; Katada, J.; Wada, A.; Takei, T.; Nishi, M.; et al. Highly specific monoclonal antibodies and epitope identification against SARS-CoV-2 nucleocapsid protein for antigen detection tests. *Cell Rep. Med.* **2021**, *2*, No. 100311.

(16) Hodge, C. D.; Rosenberg, D. J.; Grob, P.; Wilamowski, M.; Joachimiak, A.; Hura, G. L.; Hammel, M. Rigid Monoclonal Antibodies Improve Detection of SARS-CoV-2 Nucleocapsid Protein. In *MAbs*; Taylor & Francis, 2021; p 1905978.

(17) Grzelak, L.; Temmam, S.; Planchais, C.; Demeret, C.; Tondeur, L.; Huon, C.; Guivel-Benhassine, F.; Staropoli, I.; Chazal, M.; Dufloo, J. A comparison of four serological assays for detecting anti−SARS-

CoV-2 antibodies in human serum samples from different populations. *Sci. Transl. Med.* **2020**, *12*, No. eabc3103.
(18) Torres, M. D.; de Araujo, W. R.; de Lima, L. F.; Ferreira, A. L.; de la Fuente-Nunez, C. Low-cost biosensor for rapid detection of SARS-CoV-2 at the point of care. *Matter* **2021**, *4*, 2403−2416.
(19) Thudium, R. F.; Stoico, M. P.; Høgdall, E.; Høgh, J.; Krarup, H. B.; Larsen, M. A.; Madsen, P. H.; Nielsen, S. D.; Ostrowski, S. R.; Palombini, A.; et al. Early laboratory diagnosis of COVID-19 by antigen detection in blood samples of the SARS-COV-2 nucleocapsid protein. *J. Clin. Microbiol.* **2021**, *59*, No. e01001-21.
(20) Fabiani, L.; Saroglia, M.; Galatà, G.; De Santis, R.; Fillo, S.; Luca, V.; Faggioni, G.; D'Amore, N.; Regalbuto, E.; Salvatori, P.; et al. Magnetic beads combined with carbon black-based screen-printed electrodes for COVID-19: A reliable and miniaturized electrochemical immunosensor for SARS-CoV-2 detection in saliva. *Biosens. Bioelectron.* **2021**, *171*, No. 112686.
(21) Li, J.; Lillehoj, P. B. Microfluidic magneto immunosensor for rapid, high sensitivity measurements of SARS-CoV-2 Nucleocapsid protein in serum. *ACS Sens.* **2021**, *6*, 1270−1278.
(22) Drain, P. K.; Ampajwala, M.; Chappel, C.; Gvozden, A. B.; Hoppers, M.; Wang, M.; Rosen, R.; Young, S.; Zissman, E.; Montano, M. A Rapid, High-Sensitivity SARS-CoV-2 Nucleocapsid Immunoassay to Aid Diagnosis of Acute COVID-19 at the Point of Care: A Clinical Performance Study. *Infect. Dis. Ther.* **2021**, *10*, 753−761.
(23) Diao, B.; Wen, K.; Zhang, J.; Chen, J.; Han, C.; Chen, Y.; Wang, S.; Deng, G.; Zhou, H.; Wu, Y. Accuracy of a nucleocapsid protein antigen rapid test in the diagnosis of SARS-CoV-2 infection. *Clin. Microbiol. Infect.* **2021**, *27*, 289.e1−289.e4.
(24) Mboumba Bouassa, R.-S.; Veyer, D.; Péré, H.; Bélec, L. Analytical performances of the point-of-care SIENNA COVID-19 Antigen Rapid Test for the detection of SARS-CoV-2 nucleocapsid protein in nasopharyngeal swabs: A prospective evaluation during the COVID-19 second wave in France. *Int. J. Infect. Dis.* **2021**, *106*, 8−12.
(25) Jain, S.; Nehra, M.; Kumar, R.; Dilbaghi, N.; Hu, T. Y.; Kumar, S.; Kaushik, A.; Li, C.-z. Internet of medical things (IoMT)-integrated biosensors for point-of-care testing of infectious diseases. *Biosens. Bioelectron.* **2021**, *179*, No. 113074.
(26) Kaushik, A. K.; Dhau, J. S.; Gohel, H.; Mishra, Y. K.; Kateb, B.; Kim, N.-Y.; Goswami, D. Y. Electrochemical SARS-CoV-2 sensing at point-of-care and artificial intelligence for intelligent COVID-19 management. *ACS Appl. Bio Mater.* **2020**, *3*, 7306−7325.
(27) Balaji, A.; Maurya, S.; Kumar, S. Smartphone-based electrochemical sensor for assessing COVID-19 infected patients. *Int. J. Pervasive Comput. Commun.* **2020**, 1742−7371.
(28) Urso, M.; Tumino, S.; Bruno, E.; Bordonaro, S.; Marletta, D.; Loria, G. R.; Avni, A.; Shacham-Diamand, Y.; Priolo, F.; Mirabella, S. Ultrasensitive Electrochemical Impedance Detection of Mycoplasma agalactiae DNA by Low-Cost and Disposable Au-Decorated NiO Nanowall Electrodes. *ACS Appl. Mater. Interfaces* **2020**, *12*, 50143−50151.
(29) Tran, V. V.; Tran, N. H. T.; Hwang, H. S.; Chang, M. Development strategies of conducting polymer-based electrochemical biosensors for virus biomarkers: Potential for rapid COVID-19 detection. *Biosens. Bioelectron.* **2021**, *182*, No. 113192.
(30) Elbadawi, M.; Ong, J. J.; Pollard, T. D.; Gaisford, S.; Basit, A. W. Additive manufacturable materials for electrochemical biosensor electrodes. *Adv. Funct. Mater.* **2021**, *31*, No. 2006407.
(31) Neumann, B.; Wollenberger, U. Electrochemical Biosensors Employing Natural and Artificial Heme Peroxidases on Semiconductors. *Sensors* **2020**, *20*, No. 3692.
(32) Menon, S.; Mathew, M. R.; Sam, S.; Keerthi, K.; Kumar, K. G. Recent advances and challenges in electrochemical biosensors for emerging and re-emerging infectious diseases. *J. Electroanal. Chem.* **2020**, *878*, No. 114596.
(33) Farzin, L.; Sadjadi, S.; Sheini, A.; Mohagheghpour, E. A nanoscale genosensor for early detection of COVID-19 by voltammetric determination of RNA-dependent RNA polymerase (RdRP) sequence of SARS-CoV-2 virus. *Microchim. Acta* **2021**, *188*, No. 121.
(34) Ranjan, P.; Singhal, A.; Yadav, S.; Kumar, N.; Murali, S.; Sanghi, S. K.; Khan, R. Rapid diagnosis of SARS-CoV-2 using potential point-of-care electrochemical immunosensor: Toward the future prospects. *Int. Rev. Immunol.* **2021**, *40*, 126−142.
(35) Mahshid, S. S.; Flynn, S. E.; Mahshid, S. The potential application of electrochemical biosensors in the COVID-19 pandemic: A perspective on the rapid diagnostics of SARS-CoV-2. *Biosens. Bioelectron.* **2021**, *176*, No. 112905.
(36) Raziq, A.; Kidakova, A.; Boroznjak, R.; Reut, J.; Öpik, A.; Syritski, V. Development of a portable MIP-based electrochemical sensor for detection of SARS-CoV-2 antigen. *Biosens. Bioelectron.* **2021**, *178*, No. 113029.
(37) Eissa, S.; Zourob, M. Development of a low-cost cotton-tipped electrochemical immunosensor for the detection of SARS-CoV-2. *Anal. Chem.* **2021**, *93*, 1826−1833.
(38) Chen, F.-E.; Lee, P.-W.; Trick, A. Y.; Park, J. S.; Chen, L.; Shah, K.; Mostafa, H.; Carroll, K. C.; Hsieh, K.; Wang, T.-H. Point-of-Care CRISPR-Cas-Assisted SARS-CoV-2 Detection in an Automated and Portable Droplet Magnetofluidic Device. *Biosens. Bioelectron.* **2021**, *190*, No. 113390.
(39) Afroj, S.; Britnell, L.; Hasan, T.; Andreeva, D. V.; Novoselov, K. S.; Karim, N. Graphene-Based Technologies for Tackling COVID-19 and Future Pandemics. *Adv. Funct. Mater.* **2021**, *31*, No. 2107407.
(40) Kumar, S.; Chatterjee, K. Comprehensive review on the use of graphene-based substrates for regenerative medicine and biomedical devices. *ACS Appl. Mater. Interfaces* **2016**, *8*, 26431−26457.
(41) Huang, N.; Zhang, S.; Yang, L.; Liu, M.; Li, H.; Zhang, Y.; Yao, S. Multifunctional electrochemical platforms based on the Michael addition/Schiff base reaction of polydopamine modified reduced graphene oxide: construction and application. *ACS Appl. Mater. Interfaces* **2015**, *7*, 17935−17946.
(42) Zhang, S.; Huang, N.; Lu, Q.; Liu, M.; Li, H.; Zhang, Y.; Yao, S. A double signal electrochemical human immunoglobulin G immunosensor based on gold nanoparticles-polydopamine functionalized reduced graphene oxide as a sensor platform and AgNPs/carbon nanocomposite as signal probe and catalytic substrate. *Biosens. Bioelectron.* **2016**, *77*, 1078−1085.
(43) Kumar, S.; Ahlawat, W.; Kumar, R.; Dilbaghi, N. Graphene, carbon nanotubes, zinc oxide and gold as elite nanomaterials for fabrication of biosensors for healthcare. *Biosens. Bioelectron.* **2015**, *70*, 498−503.
(44) Aykaç, A.; Gergeroglu, H.; Beşli, B.; Akkaş, E. Ö.; Yavaş, A.; Güler, S.; Güneş, F.; Erol, M. An Overview on Recent Progress of Metal Oxide/Graphene/CNTs-Based Nanobiosensors. *Nanoscale Res. Lett.* **2021**, *16*, No. 65.
(45) Zhang, S.; Li, R.; Liu, X.; Yang, L.; Lu, Q.; Liu, M.; Li, H.; Zhang, Y.; Yao, S. A novel multiple signal amplifying immunosensor based on the strategy of in situ-produced electroactive substance by ALP and carbon-based Ag-Au bimetallic as the catalyst and signal enhancer. *Biosens. Bioelectron.* **2017**, *92*, 457−464.
(46) Napi, M. L. M.; Sultan, S. M.; Ismail, R.; How, K. W.; Ahmad, M. K. Electrochemical-based biosensors on different zinc oxide nanostructures: A review. *Materials* **2019**, *12*, No. 2985.
(47) Sharma, A.; Agrawal, A.; Kumar, S.; Awasthi, K. K.; Awasthi, K.; Awasthi, A. Zinc Oxide Nanostructures−Based Biosensors. In *Nanostructured Zinc Oxide*; Elsevier, 2021; Vol. *564−565*, pp 655−695.
(48) Zhu, Q.; Cai, F.; Zhang, J.; Zhao, K.; Deng, A.; Li, J. Highly sensitive electrochemiluminescent immunosensor based on gold nanoparticles-functionalized zinc oxide nanorod and poly (amido-amine)-graphene for detecting brombuterol. *Biosens. Bioelectron.* **2016**, *86*, 899−906.
(49) Wu, Q.; Hou, Y.; Zhang, M.; Hou, X.; Xu, L.; Wang, N.; Wang, J.; Huang, W. Amperometric cholesterol biosensor based on zinc oxide films on a silver nanowire−graphene oxide modified electrode. *Anal. Methods* **2016**, *8*, 1806−1812.
(50) Zhang, T.; Gu, Y.; Li, C.; Yan, X.; Lu, N.; Liu, H.; Zhang, Z.; Zhang, H. Fabrication of novel electrochemical biosensor based on graphene nanohybrid to detect H2O2 released from living cells with

ultrahigh performance. *ACS Appl. Mater. Interfaces* **2017**, *9*, 37991−37999.
(51) Wan, S.; Jiang, L.; Cheng, Q. Design principles of high-performance graphene films: interfaces and alignment. *Matter* **2020**, *3*, 696−707.
(52) Torrente-Rodríguez, R. M.; Tu, J.; Yang, Y.; Min, J.; Wang, M.; Song, Y.; Yu, Y.; Xu, C.; Ye, C.; IsHak, W. W.; et al. Investigation of cortisol dynamics in human sweat using a graphene-based wireless mHealth system. *Matter* **2020**, *2*, 921−937.
(53) Niu, Y.; Xie, H.; Luo, G.; Zhuang, Y.; Wu, X.; Li, G.; Sun, W. ZnO-reduced graphene oxide composite based photoelectrochemical aptasensor for sensitive Cd (II) detection with methylene blue as sensitizer. *Anal. Chim. Acta* **2020**, *1118*, 1−8.
(54) Zhao, Y.; Li, W.; Pan, L.; Zhai, D.; Wang, Y.; Li, L.; Cheng, W.; Yin, W.; Wang, X.; Xu, J.-B. ZnO-nanorods/graphene heterostructure: a direct electron transfer glucose biosensor. *Sci. Rep.* **2016**, *6*, No. 32327.
(55) Salih, E.; Mekawy, M.; Hassan, R. Y.; El-Sherbiny, I. M. Synthesis, characterization and electrochemical-sensor applications of zinc oxide/graphene oxide nanocomposite. *J. Nanostruct. Chem.* **2016**, *6*, 137−144.
(56) Hwa, K.-Y.; Subramani, B. Synthesis of zinc oxide nanoparticles on graphene−carbon nanotube hybrid for glucose biosensor applications. *Biosens. Bioelectron.* **2014**, *62*, 127−133.
(57) Mazaheri, M.; Aashuri, H.; Simchi, A. Three-dimensional hybrid graphene/nickel electrodes on zinc oxide nanorod arrays as non-enzymatic glucose biosensors. *Sens. Actuators, B* **2017**, *251*, 462−471.
(58) Chen, H.-C.; Su, W.-R.; Yeh, Y.-C. Functional channel of SWCNTs/Cu2O/ZnO NRs/graphene hybrid electrodes for highly sensitive nonenzymatic glucose sensors. *ACS Appl. Mater. Interfaces* **2020**, *12*, 32905−32914.
(59) Zhu, D.; Ma, H.; Zhen, Q.; Xin, J.; Tan, L.; Zhang, C.; Wang, X.; Xiao, B. Hierarchical flower-like zinc oxide nanosheets in-situ growth on three-dimensional ferrocene-functionalized graphene framework for sensitive determination of epinephrine and its oxidation derivative. *Appl. Surf. Sci.* **2020**, *526*, No. 146721.
(60) Pan, Y.; Zuo, J.; Hou, Z.; Huang, Y.; Huang, C. Preparation of electrochemical sensor based on zinc oxide nanoparticles for simultaneous determination of AA, DA, and UA. *Front. Chem.* **2020**, *8*, No. 892.
(61) Wang, Y.-W.; Cao, A.; Jiang, Y.; Zhang, X.; Liu, J.-H.; Liu, Y.; Wang, H. Superior antibacterial activity of zinc oxide/graphene oxide composites originating from high zinc concentration localized around bacteria. *ACS Appl. Mater. Interfaces* **2014**, *6*, 2791−2798.
(62) Aditya, A.; Chattopadhyay, S.; Jha, D.; Gautam, H. K.; Maiti, S.; Ganguli, M. Zinc oxide nanoparticles dispersed in ionic liquids show high antimicrobial efficacy to skin-specific bacteria. *ACS Appl. Mater. Interfaces* **2018**, *10*, 15401−15411.
(63) Vabbina, P. K.; Kaushik, A.; Pokhrel, N.; Bhansali, S.; Pala, N. Electrochemical cortisol immunosensors based on sonochemically synthesized zinc oxide 1D nanorods and 2D nanoflakes. *Biosens. Bioelectron.* **2015**, *63*, 124−130.
(64) Martins, B. R.; Sampaio, T. M.; de Farias, A. K. S. R.; de Paula Martins, R.; Teixeira, R. R.; Oliveira, R. T. S.; Oliveira, C. J. F.; da Silva, M. V.; Rodrigues, V.; Dantas, N. O.; et al. Immunosensor Based on Zinc Oxide Nanocrystals Decorated with Copper for the Electrochemical Detection of Human Salivary Alpha-Amylase. *Micromachines* **2021**, *12*, No. 657.
(65) Xie, L.; Xu, Y.; Cao, X. Hydrogen peroxide biosensor based on hemoglobin immobilized at graphene, flower-like zinc oxide, and gold nanoparticles nanocomposite modified glassy carbon electrode. *Colloids Surf., B* **2013**, *107*, 245−250.
(66) Hatami, Z.; Ragheb, E.; Jalali, F.; Tabrizi, M. A.; Shamsipur, M. Zinc oxide-gold nanocomposite as a proper platform for label-free DNA biosensor. *Bioelectrochemistry* **2020**, *133*, No. 107458.
(67) Low, S. S.; Tan, M. T.; Loh, H.-S.; Khiew, P. S.; Chiu, W. S. Facile hydrothermal growth graphene/ZnO nanocomposite for development of enhanced biosensor. *Anal. Chim. Acta* **2016**, *903*, 131−141.
(68) Low, S. S.; Loh, H.-S.; Boey, J. S.; Khiew, P. S.; Chiu, W. S.; Tan, M. T. Sensitivity enhancement of graphene/zinc oxide nanocomposite-based electrochemical impedance genosensor for single stranded RNA detection. *Biosens. Bioelectron.* **2017**, *94*, 365−373.
(69) Verma, S.; Singh, S. P. Non-invasive oral cancer detection from saliva using zinc oxide−reduced graphene oxide nanocomposite based bioelectrode. *MRS Commun.* **2019**, *9*, 1227−1234.
(70) A Karim, S. S.; Nadzirah, S.; Kazmi, J.; Rahim, R. A.; Dee, C. F.; Hamzah, A. A.; Mohamed, M. A. Zinc oxide nanorods-based immuno-field-effect transistor for human serum albumin detection. *J. Mater. Sci.* **2021**, *56*, 15344−15353.
(71) Myndrul, V.; Coy, E.; Bechelany, M.; Iatsunskyi, I. Photoluminescence label-free immunosensor for the detection of Aflatoxin B1 using polyacrylonitrile/zinc oxide nanofibers. *Mater. Sci. Eng., C* **2021**, *118*, No. 111401.
(72) Liu, B.; Liu, J. Interface-driven hybrid materials based on DNA-functionalized gold nanoparticles. *Matter* **2019**, *1*, 825−847.
(73) Vashist, S. K.; Lam, E.; Hrapovic, S.; Male, K. B.; Luong, J. H. Immobilization of antibodies and enzymes on 3-aminopropyltriethoxysilane-functionalized bioanalytical platforms for biosensors and diagnostics. *Chem. Rev.* **2014**, *114*, 11083−11130.
(74) Zhang, Q.; Park, K.; Cao, G. Synthesis of ZnO aggregates and their application in dye-sensitized solar cells. *Mater. Matters* **2010**, *5*, 32−38.
(75) Srivastava, S.; Abraham, S.; Singh, C.; Ali, M. A.; Srivastava, A.; Sumana, G.; Malhotra, B. D. Protein conjugated carboxylated gold@reduced graphene oxide for aflatoxin B 1 detection. *RSC Adv.* **2015**, *5*, 5406−5414.
(76) Neelgund, G. M.; Oki, A. Cobalt phthalocyanine-sensitized graphene−ZnO composite: An efficient near-infrared-active photothermal agent. *ACS Omega* **2019**, *4*, 5696−5704.
(77) Faniyi, I.; Fasakin, O.; Olofinjana, B.; Adekunle, A.; Oluwasusi, T.; Eleruja, M.; Ajayi, E. The comparative analyses of reduced graphene oxide (RGO) prepared via green, mild and chemical approaches. *SN Appl. Sci.* **2019**, *1*, No. 0144842.
(78) Galande, C.; Mohite, A. D.; Naumov, A. V.; Gao, W.; Ci, L.; Ajayan, A.; Gao, H.; Srivastava, A.; Weisman, R. B.; Ajayan, P. M. Quasi-molecular fluorescence from graphene oxide. *Sci. Rep.* **2011**, *1*, No. 85.
(79) Miletto, I.; Catizzone, E.; Bonura, G.; Ivaldi, C.; Migliori, M.; Gianotti, E.; Marchese, L.; Frusteri, F.; Giordano, G. In situ FT-IR characterization of CuZnZr/ferrierite hybrid catalysts for one-pot CO2-to-DME conversion. *Materials* **2018**, *11*, No. 2275.
(80) Neelgund, G. M.; Oki, A. Graphene-coupled zno: A robust nir-induced catalyst for rapid photo-oxidation of cyanide. *ACS Omega* **2017**, *2*, 9095−9102.
(81) Ashkenov, N.; Mbenkum, B.; Bundesmann, C.; Riede, V.; Lorenz, M.; Spemann, D.; Kaidashev, E.; Kasic, A.; Schubert, M.; Grundmann, M.; et al. Infrared dielectric functions and phonon modes of high-quality ZnO films. *J. Appl. Phys.* **2003**, *93*, 126−133.
(82) Lin, K.-F.; Cheng, H.-M.; Hsu, H.-C.; Hsieh, W.-F. Band gap engineering and spatial confinement of optical phonon in ZnO quantum dots. *Appl. Phys. Lett.* **2006**, *88*, No. 263117.
(83) Li, J.; Li, H. Physical and electrical performance of vapor−solid grown ZnO straight nanowires. *Nanoscale Res. Lett.* **2009**, *4*, 165−168.
(84) Dong, X.; Cao, Y.; Wang, J.; Chan-Park, M. B.; Wang, L.; Huang, W.; Chen, P. Hybrid structure of zinc oxide nanorods and three dimensional graphene foam for supercapacitor and electrochemical sensor applications. *RSC Adv.* **2012**, *2*, 4364−4369.
(85) Muralikrishna, S.; Sureshkumar, K.; Varley, T. S.; Nagaraju, D. H.; Ramakrishnappa, T. In situ reduction and functionalization of graphene oxide with L-cysteine for simultaneous electrochemical determination of cadmium (II), lead (II), copper (II), and mercury (II) ions. *Anal. Methods* **2014**, *6*, 8698−8705.
(86) Kashinath, L.; Namratha, K.; Byrappa, K. Microwave assisted synthesis and characterization of nanostructure zinc oxide-graphene

https://doi.org/10.1021/acsami.1c24475
ACS Appl. Mater. Interfaces 2022, 14, 10844−10855

oxide and photo degradation of brilliant blue. *Mater. Today: Proc.* **2016**, *3*, 74−83.
(87) Maduraiveeran, G.; Sasidharan, M.; Ganesan, V. Electrochemical sensor and biosensor platforms based on advanced nanomaterials for biological and biomedical applications. *Biosens. Bioelectron.* **2018**, *103*, 113−129.
(88) Wang, K.; Ruan, J.; Song, H.; Zhang, J.; Wo, Y.; Guo, S.; Cui, D. Biocompatibility of graphene oxide. *Nanoscale Res. Lett.* **2011**, *6*, No. 8.
(89) Mohammadkhani, R.; Ramezanzadeh, M.; Saadatmandi, S.; Ramezanzadeh, B. Designing a dual-functional epoxy composite system with self-healing/barrier anti-corrosion performance using graphene oxide nano-scale platforms decorated with zinc doped-conductive polypyrrole nanoparticles with great environmental stability and non-toxicity. *Chem. Eng. J.* **2020**, *382*, No. 122819.
(90) Phiri, J.; Johansson, L.-S.; Gane, P.; Maloney, T. A comparative study of mechanical, thermal and electrical properties of graphene-, graphene oxide-and reduced graphene oxide-doped microfibrillated cellulose nanocomposites. *Composites, Part B* **2018**, *147*, 104−113.
(91) Kakaei, K.; Esrafili, M. D.; Ehsani, A. Characterization. In *Interface Science and Technology*; Elsevier, 2019; Vol. *27*, pp 109−151.
(92) Torrente-Rodríguez, R. M.; Lukas, H.; Tu, J.; Min, J.; Yang, Y.; Xu, C.; Rossiter, H. B.; Gao, W. SARS-CoV-2 RapidPlex: a graphene-based multiplexed telemedicine platform for rapid and low-cost COVID-19 diagnosis and monitoring. *Matter* **2020**, *3*, 1981−1998.
(93) Eissa, S.; Alhadrami, H. A.; Al-Mozaini, M.; Hassan, A. M.; Zourob, M. Voltammetric-based immunosensor for the detection of SARS-CoV-2 nucleocapsid antigen. *Microchim. Acta* **2021**, *188*, No. 199.
(94) Lee, J.-H.; Choi, M.; Jung, Y.; Lee, S. K.; Lee, C.-S.; Kim, J.; Kim, J.; Kim, N. H.; Kim, B.-T.; Kim, H. G. A novel rapid detection for SARS-CoV-2 spike 1 antigens using human angiotensin converting enzyme 2 (ACE2). *Biosens. Bioelectron.* **2021**, *171*, No. 112715.
(95) Crescenzo-Chaigne, B.; Behillil, S.; Enouf, V.; Escriou, N.; Petres, S.; Ungeheuer, M. N.; Ghosn, J.; Tubiana, S.; Bouadma, L.; van der Werf, S. Nasopharyngeal and serological anti SARS-CoV-2 IgG/IgA responses in COVID-19 patients. *medRxiv* **2021**, *1*, No. 100041.
(96) Gremmels, H.; Winkel, B. M.; Schuurman, R.; Rosingh, A.; Rigter, N. A.; Rodriguez, O.; Ubijaan, J.; Wensing, A. M.; Bonten, M. J.; Hofstra, L. M. Real-life validation of the Panbio COVID-19 antigen rapid test (Abbott) in community-dwelling subjects with symptoms of potential SARS-CoV-2 infection. *EClinicalMedicine* **2021**, *31*, No. 100677.

https://doi.org/10.1021/acsami.1c24475
ACS Appl. Mater. Interfaces 2022, 14, 10844−10855